# Direct Digital Control of Single-Phase Grid-Connected Inverters With *LCL* Filter Based on Inductance Estimation Model

Tsai-Fu Wu, *Senior Member, IEEE*, Mitradatta Misra, Ying-Yi Jhang, Yen-Hsiang Huang, and Li-Chiun Lin

***Abstract*—Soft magnetic powder cores with their high saturation flux density and low core loss are excellent alternatives for filter inductors in inverter-based applications. However, their nonlinear current-dependent inductance characteristics pose a challenge for control of grid-connected inverter with *LCL* filter. In this paper, the variable inductance conundrum is discussed and a modified direct digital control method based on a variable-structure inductance estimation model that takes into consideration wide nonlinear variation in both inverter- and grid-side inductances is proposed. The proposed method is shown to have better grid-voltage harmonic rejection and improved stability margins. However, investigation of stability which is conventionally based on nominal values of filter inductors cannot predict instabilities over the entire range of inductance variation. Hence, a parametric approach to conventional stability methods with a parameter space defined by variation in actual and estimated inductance is explored in this paper. The effect of line impedance on stability is also investigated with impedance-based stability criterion by considering line inductance as an additional dimension in the parameter space. A pattern in stability margins is observed due to inductance variation, with inductance at its minimum being most vulnerable to instability. Experimental results measured from a 5 kW single-phase grid-connected inverter with various *LCL* filters have verified the feasibility of the proposed control method. The experimental results also match the analytical results with reasonable accuracy.**

***Index Terms*—Damping, direct digital control, harmonics, inductance variation, inverter, *LCL* filter, line impedance, magnetic permeability, resonant frequency, stability.**

## I. Introduction

INTERFACING low-pass filters is essential to grid-connected inverters for delivering power with quality in accordance to regulatory standards [1], [2]. A natural progression from simple

Manuscript received September 12, 2017; revised December 22, 2017 and March 20, 2018; accepted April 19, 2018. Date of publication April 26, 2018; date of current version December 7, 2018. This work was supported by the Ministry of Science and Technology, Taiwan. Recommended for publication by Associate Editor L. Peng. *(Corresponding author: Tsai-Fu Wu.)*

T.-F. Wu is with the Elegant Power Application Center, National Chung Cheng University, Chia-Yi 62102, Taiwan (e-mail:

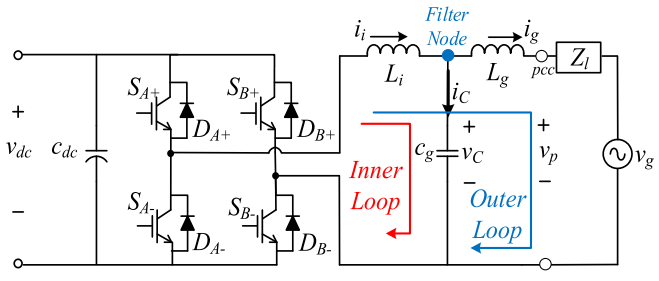


Fig. 1. Single-phase bidirectional inverter with an *LCL* filter.

operating points. A parameter space defined by maximum allowable drop in inductance and expected variation in inductance estimation is used to observe the stability margins for controller's current tracking capability using conventional bode plots. However, the controller is also affected by variations in terminal voltage because of control-output impedance interaction with line impedance. Hence, the line impedance is added as an additional dimension to the parameter space and impedance-based stability analysis method [33] is applied to observe the effect of line impedance under filter inductance variation. Analytical results have shown to be in good agreement with experimental results, confirming the applicability of parametric approach to conventional stability analysis methods under filter inductance variation.

This paper is organized as follows: The variable inductance conundrum is discussed in Section II. The basic direct digital control law and the necessary modifications for *LCL* filter are presented in Section III. The modified inductance estimation model to deal with large signal stability is elaborated in Section IV. A comprehensive treatment to stability analysis is done in Section V. Finally, experimental validation of the controller from a 5 kW single-phase grid-connected inverter, as shown in Fig. 1, is presented in Section VI.

## II. Variable Inductance Conundrum

When filter inductance shows a wide variation with current at line frequency $f_0$ due to core's nonlinear permeability characteristics, the natural question that arises is: "Should the inductor be treated as operating with 0 dc-bias and ac at line frequency $f_0$ and switching frequency $f_s$ or, each point along the steady-state trajectory of current at $f_0$ should be treated as dc-bias with current at $f_s$ superimposed on the dc-bias?" An intuitive answer lies in the understanding of basic operation of switch-mode power supplies (SMPS). The inductor current in inverters could be seen as, not exactly an ac at $f_0$, rather as a series of magnetizing and demagnetizing currents at $f_s$. Since $f_s \gg f_0$, the voltage across the filter inductor can be treated to be relatively constant in each switching cycle. Thus, the inductor in each switching cycle could be seen to be operating with the following characteristics.

1) A dc-bias, which is actually the instantaneous ac at $f_0$.
2) An ac at $f_s$ superimposed on the dc-bias, corresponds to the magnetizing and demagnetizing currents at $f_s$ due to the switching nature of SMPSs.
3) A small change in the dc-bias because of unequal magnetizing and demagnetizing currents at $f_s$, which is the basic control nature of inverters.

Now, this necessitates a reconsideration of the expression for voltage across an inductor, which otherwise is derived with assumption of constant permeability. The following derivation is based on fundamental laws of physics found in classical textbooks [30] and reiterated for the sake of completeness. The voltage $v_{Lx}$ across an inductor $L_x$ based on Faraday's law of electromagnetic induction is given by the following:

$$v_{Lx} = N\frac{d\emptyset_x}{dt} \tag{1}$$

where the subscript $x \in \{i,\ g\}$ refers to inverter- or grid-side, respectively, $N$ is the number of turns of inductor coil, and $\emptyset_x$ is the associated magnetic flux given by the following:

$$\emptyset_x = B_x\ A \tag{2}$$

where $B_x$ is the magnetic flux density that is assumed to be constant over the area $A$ under consideration and expressed as follows:

$$B_x = \mu\left(i_x\right) H_x \tag{3}$$

where $\mu$ is the magnetic permeability of the inductor core, which is a nonlinear function of current $i_x$ through the inductor [31] and $H_x$ is the magnetic field strength given by Ampere's circuital law

$$H_x = \frac{Ni_x}{l} \tag{4}$$

with the assumption of constant $H_x$ along the length $l$ of the inductor coil. Thus, from (1)–(4), the expression for $v_{Lx}$ is derived to be as follows:

$$v_{Lx} = \frac{N^2 A}{l}\ \frac{d\mu\left(i_x\right) i_x}{dt}. \tag{5}$$

When we choose an operating point along the steady-state trajectory of current $i_x$, (5) could be expressed as follows:

$$v_{Lx} = \frac{N^2 A}{l}\ \frac{d}{dt}\left\{\mu\left(I_x + \widehat{i_x}\right)\left(I_x + \widehat{i_x}\right)\right\} \tag{6}$$

where $I_x$ is the dc-bias and $\widehat{i_x}$ is the small-signal perturbation around $I_x$. Assuming $\mu\left(I_x + \widehat{i_x}\right) = \mu_{\rm dc}\left(I_x\right) + \mu_{\rm ac}(\widehat{i_x})$, where $\mu_{\rm dc}(I_x)$ refers to a constant dc-permeability and $\mu_{\rm ac}(\widehat{i_x})$ to a variable ac-permeability [31], (6) can be further expanded as follows:

$$v_{Lx} = \frac{N^2 A}{l}\ \left\{\mu_{\rm dc}\left(I_x\right)\frac{di_x}{dt} + I_x\frac{d\mu_{\rm ac}\left(\widehat{i_x}\right)}{dt} + \frac{d}{dt}\mu_{\rm ac}\left(\widehat{i_x}\right)\widehat{i_x}\right\}. \tag{7}$$

The value for $\mu_{\rm dc}(I_x)$ in the first term of (7) can be derived from permeability versus dc-bias curves in core-manufacturer's datasheets [34], [35], as shown in Fig. 2(a), while the second term in (7) can be considered negligible because the slope of permeability versus ac curves for small values of ac is usually close to 0, [35], as shown in Fig. 2(b). And finally, the third term in (7) can also be neglected because of its second-order nature

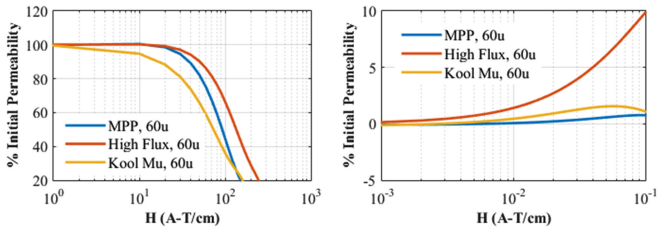


Fig. 2. Permeability curves for typical cores. (a) Permeability versus dc-bias. (b) Permeability versus ac flux density.

in small-signal sense. Thus, the expression for $v_{Lx}$ is simplified to the following:

$$v_{Lx} = \frac{N^2 A \mu_{\rm dc}\left(I_x\right)}{l}\ \frac{di_x}{dt} = L_x\ \left(I_x\right)\frac{di_x}{dt} \tag{8}$$

with $L_x(I_x)$ defined as instantaneous inductance at the operating point. This is equivalent to standard definition of voltage across an inductor [30], with the only difference being the value of inductance $L_x$ varies from one operating point to another. This equivalence simplifies the derivation of control law in each switching cycle and also makes conventional stability analysis methods applicable. However, the variation of inductance from one operating point to another requires the control law to be updated in every switching cycle while stability analysis be performed for the entire range of variation. The details are presented in the following sections.

## III. Review of Direct Digital Control

### A. Basic Direct Digital Control Law

Direct digital control law is based on the fundamental network theory and a filter inductance model. The basic control law [18] is derived in two steps of division and summation.

*Division (D):* In every switching cycle, the inverter-side inductor $L_i$ has two operation states, magnetization and demagnetization. Applying KVL to the inner loop, shown in Fig. 1, the following state equations can be derived:

$$\Delta\, i_{i,\rm mag} = \frac{v_{\rm dc} - v_c}{L_i}\, dT_s \tag{9}$$

and

$$\Delta\, i_{i,\rm dem} = -\frac{v_{\rm dc} + v_c}{L_i}\left(1-d\right)T_s, \tag{10}$$

where $\Delta i_{i,\rm mag}$ and $\Delta i_{i,\rm dem}$ are the inverter-side current $i_i$ variation during magnetization and demagnetization, respectively, and $d$ is the duty ratio, $T_s$ is the switching period, $v_{\rm dc}$ is the dc-link voltage, and $v_c$ is the filter capacitor voltage.

*Summation ($\Sigma$):* The total inverter-side inductor current variation $\Delta i_i$ in one switching cycle is obtained by adding the two state equations (9) and (10) as shown in the following:

$$\Delta i_i = \frac{2v_{\rm dc}T_s}{L_i}\, d - \frac{v_{\rm dc} + v_c}{L_i}T_s. \tag{11}$$

Thus, the basic control law is derived from (11) as follows:

$$d = \frac{1}{2} + \frac{v_c}{2v_{\rm dc}} + \frac{L_i}{2v_{\rm dc}T_s}\Delta i_i. \tag{12}$$

The filter inductance value is estimated from a current-dependent nonlinear inductance model and acts as an adaptive proportionality factor. This ensures wide variation in inverter-side inductance is dynamically taken into consideration without any further proportionality factor tuning. However, wide variation in both inverter- and grid-side inductances needs to be considered with *LCL* filters. Moreover, *LCL* filters being more vulnerable to instability require additional compensation. Hence, a modified control law is derived to overcome the limitations of basic control.

### B. Modified Direct Digital Control Law

The modified control law for *LCL* filter is derived similarly by applying KVL to the outer loop and KCL to filter node, shown in Fig. 1, in two steps of division and summation.

*Division (D):* The expressions for inverter-side current variation during magnetization and demagnetization are as follows:

$$\Delta\, i_{i,\rm mag} = \frac{v_{\rm dc} - v_P}{L_i + L_g}\, dT_s + \frac{L_g}{L_i + L_g}\Delta i_{c,\rm mag} \tag{13}$$

and

$$\Delta\, i_{i,\rm dem} = -\frac{v_{\rm dc} + v_P}{L_i + L_g}\left(1-d\right)T_s + \frac{L_g}{L_i + L_g}\Delta i_{c,\rm dem} \tag{14}$$

where $\Delta i_{c,\rm mag}$ and $\Delta i_{c,\rm dem}$ are the corresponding variation in filter-capacitor current $i_c$ and $v_P$ is the voltage at the point of common coupling (PCC).

*Summation ($\Sigma$):* The total inverter-side current variation is as follows:

$$\Delta\, i_i = \frac{2v_{\rm dc}T_s}{L_i + L_g}\, d - \frac{v_{\rm dc} + v_P}{L_i + L_g}T_s + \frac{L_g}{L_i + L_g}\Delta i_c. \tag{15}$$

A control law in discrete-time domain is derived from (15) by considering the following.

1) The total current difference $\Delta i_i$ to be the sum of reference current difference for next switching cycle (i.e., $i_{\rm ref}(n+1) - i_{\rm ref}(n)$, which is equivalent to reference current feedforward) and current tracking error (i.e., $i_{\rm ref}(n) - i_i(n)$) for the current switching cycle [18], [19].
2) The capacitor current difference term $\Delta i_c$ in (15) needs to be compensated so as to cancel the effect of filter capacitor [19].

Thus, the modified control law along with the compensation term in discrete time is expressed as shown in the following:

$$\begin{aligned} d\left(n+1\right) = {} & \frac{1}{2} \\ & + \frac{v_P^*\left(n\right)}{2v_{\rm dc}\left(n\right)} + L_{eT}\left(n+1\right).\frac{i_{\rm ref}\left(n+1\right) - i_i\left(n\right)}{2v_{\rm dc}\left(n\right)T_s} \\ & + \frac{L_{eg}\left(n+1\right)C_g}{2v_{\rm dc}\left(n\right)}.\frac{v_c^*\left(n\right) - 2v_c^*\left(n-1\right) + v_c^*\left(n-2\right)}{{T_s}^2} \end{aligned} \tag{16}$$

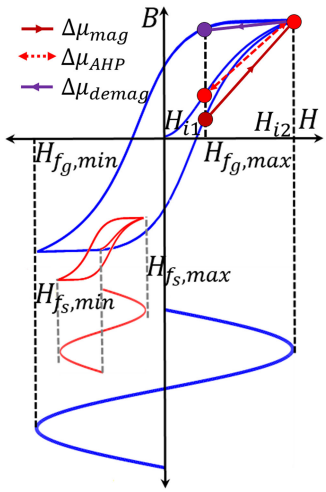


Fig. 3. Nonlinear current-dependent permeability characteristics.

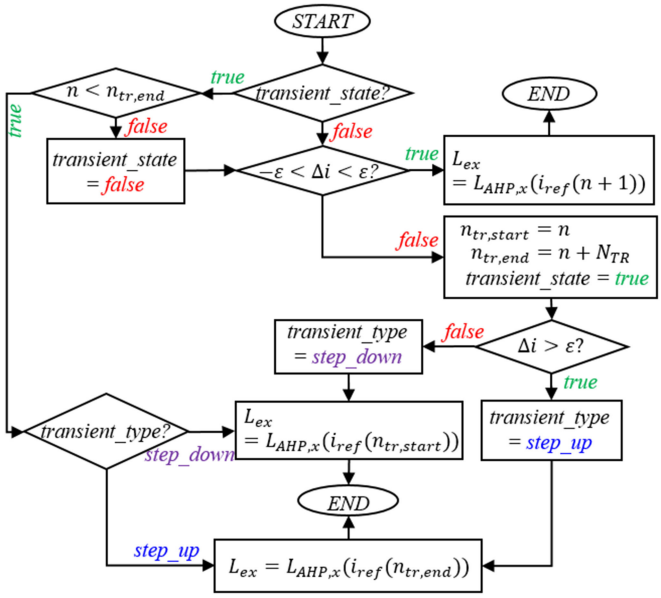


Fig. 4. Variable structure inductance estimation model.

where $n$ and $n+1$ represent the current and next switching cycle instants and $L_{eT}$ is the sum of the estimates of the inverter side $L_{ei}$ and grid side $L_{eg}$ inductances from the filter inductance model. $v_c^*$ and $v_P^*$ samples used in (16) are actually the averages of their corresponding rising-edge and falling-edge samples [37], i.e., $v_c^*(n) = 0.5(v_c(n) + v_c(n-0.5))$ and $v_P^*(n) = 0.5(v_P(n) + v_P(n-0.5))$. This method is applied to eliminate the effect of approximately $90^\circ$ phase shift between switching ripples of inductor current and terminal voltage. The last term in (16) is the compensation term corresponding to filter capacitor current difference, $\Delta i_c$ in (15). The first-order derivative of filter capacitor voltage $v_c$ using simple backward Euler method is applied to determine $i_c$. However, digital differentiators with generalized integrators [36] could also be used for higher accuracy.

## IV. Inductance Estimation Model

Inductance values are typically estimated from the anhysteretic polynomial expressions $L_{\mathrm{AHP},x}(i)$ derived from the expressions for percentage of initial permeability (dc-permeability curves) given in manufacturers' datasheets [34], [35]. However, inductors exhibit both major and minor hysteresis loops [38] as shown in Fig. 3, under steady state due to switch-mode operation, causing the estimated inductance $L_{ex}$ to vary from absolute inductance $L_x$ at any instant. The major loop corresponds to ac excitation at line frequency $f_0$ and the minor loop corresponds to that at switching frequency $f_s$. It can be seen from the major loop, shown in Fig. 3, that the incremental permeability profile (i.e., slope of the line joining the initial and final points along the curve) during a large-signal step down $\Delta\mu_{\mathrm{demag}}$ varies significantly from that during a large-signal step up $\Delta\mu_{\mathrm{mag}}$. In fact, $\Delta\mu_{\mathrm{demag}}$ is comparatively slower than $\Delta\mu_{\mathrm{mag}}$. Since, inductance is directly proportional to magnetic permeability ($L_x \propto \mu_x$), $L_x$ would vary significantly from $L_{ex}$ based on only $L_{\mathrm{AHP},x}(i)$.

The discrepancy between $L_x$ and $L_{ex}$ during steady state is increasingly becoming irrelevant due to advancements in soft magnetic material technology and also usually controllable, unless the resonant frequency due to drop in inductance reaches stability boundary [17]. And the output response during transient state would also eventually converge regardless of the aforementioned discrepancy, unless the resulting (over) undershoot hits the predefined protection limit. Hence, to ensure stability under steady-state operation, the filter parameters are chosen such that the resonant-frequency shift due to drop in inductance remains within the stability boundary [17]. And to ensure overall stability, a variable-structure inductance model loosely based on the hysteretic behavior is implemented.

Now, mathematically quantifying the observed effect of hysteresis on incremental permeability is not that simple. Hence, $L_{ex}$ is simply held at the expected final value for a fixed number of switching cycles during a large-signal step up operation, emulating fast changing incremental permeability characteristics during magnetization (see the slope in MAROON in Fig. 3). On the contrary, $L_{ex}$ is held at its initial value during a large signal step down operation, emulating slow changing incremental permeability characteristics during demagnetization (see the slope in PURPLE in Fig. 3). The expected number of switching cycles required for the incremental permeability characteristics to come back to normal after a sudden change in current $\boldsymbol{N_{TR}}$ is treated as a design parameter. A typical value of 5 to 10 switching cycles for switching frequency of 30 kHz, which is equivalent to 0.167–0.334 ms, has been observed to be a good choice for very large signal step down or step up operations, such as 5–1 kW (a drop in current from 32.14 to 6.42 A peak) or vice versa. The decision on transient or steady state is done by checking the difference between reference and feedback currents $\Delta i$ in each switching cycle. The acceptable limit on $\Delta i$ for which the effect of hysteresis can be considered to be negligible, $\varepsilon$ is also treated as a design parameter. A typical value of 10–15 A has been observed to be acceptable from experimental results. Both the choice for $N_{TR}$ and $\varepsilon$ will vary according to the choice of the inductor core. Whenever $\Delta i$ is determined to be beyond the limits defined by $\pm\varepsilon$, the transient-state start and end switching cycle instants are initialized as $n_{tr,\mathrm{start}} = n$ and $n_{tr,\mathrm{end}} = n + N_{TR}$,

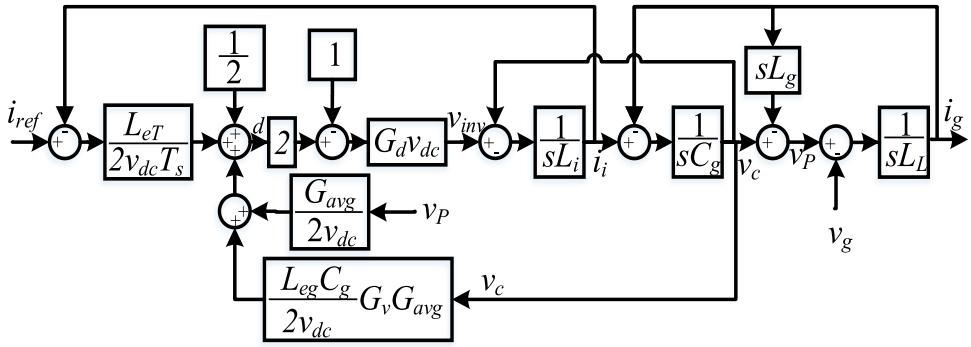


Fig. 5. Switching average model of grid-connected inverter with *LCL* filter for direct digital control with compensation operating in bipolar mode.

respectively. The reference current at $\boldsymbol{n_{tr,}}_{\text{start}}$ or $n_{tr,\text{end}}$ is then used in $L_{\text{AHP},x}(i)$ to derive $L_{ex}$ accordingly. However, under steady-state and small-signal transient-state operations, $L_{ex}$ is directly derived with reference current for next switching cycle instant from $L_{\text{AHP},x}(i)$. This estimation process is elaborated in a flowchart shown in Fig. 4.

This variable structure estimation model ensures that the control can adapt rapidly to periodically changing plant structure during steady-state operation, while also exhibit robust behavior to sudden change in the plant structure during large signal transient operation. This could be seen as a variable-structure controller [39] with estimated inductance values and hence, the controller gains depending on core and current characteristics. The significant advantage of the control method is that usually no additional proportionality constant tuning is necessary if the *LCL* filter has been designed to work within its region of stability over the entire range of filter inductance variation.

## V. Stability Analysis

Stability analysis is done using the classical switching average model [40] in *s*-domain, considering the dc-bias (i.e., instantaneous ac at $f_0$) as the operating point and ac at $f_s$ as the small-signal perturbation. The small-signal perturbation could be considered as a permanent disturbance because it also causes a change in the dc-bias, as discussed in Section II. But, it is treated as a case of stability subject to an instantaneous disturbance but operating at a new equilibrium point [41]. The time-domain switching average model of the system shown in Fig. 1, based on the discussion in Section II and assuming a bipolar operation is given by the following:

$$\begin{bmatrix} \frac{di_i}{dt} \\ \frac{dv_c}{dt} \\ \frac{di_g}{dt} \end{bmatrix} = \begin{bmatrix} 0 & -\frac{1}{L_i\,(I_i)} & 0 \\ \frac{1}{C_g} & 0 & -\frac{1}{C_g} \\ 0 & \frac{1}{L_g\,(I_g)+L_L} & 0 \end{bmatrix} \begin{bmatrix} i_i \\ v_c \\ i_g \end{bmatrix} + \begin{bmatrix} \frac{2d-1}{L_i\,(I_i)} & 0 \\ 0 & 0 \\ 0 & -\frac{1}{L_g\,(I_g)+L_L} \end{bmatrix} \begin{bmatrix} v_{\text{dc}} \\ v_g \end{bmatrix}. \quad (17)$$

The corresponding model in *s*-domain along with the controller (16) is shown in Fig. 5. The term $G_d(s)$ represents the overall delay transfer function that includes computational delay, sampler, and zero-order hold [42], $G_{\text{avg}}(s)$ represents the rising-edge and falling-edge samples averaging used for $v_c$ and $v_P$ in (16) and $G_v(s)$ is the *s*-domain representation of second-order difference equation used to derive the compensation term in (16). The expressions for $G_d(s)$, $G_{\text{avg}}(s)$, and $G_v(s)$ are as follows:

$$\begin{aligned} G_d\ (s) &= e^{-sk_dT_s}\ \left(\frac{1-e^{-sT_s}}{sT_s}\right), \qquad 0 \le k_d \le 1.0 \\ G_{\text{avg}}\ (s) &= \frac{1+e^{-s0.5T_s}}{2} \\ G_v\ (s) &= \frac{1-2e^{-sT_s}+e^{-2sT_s}}{T_s^2}. \end{aligned} \quad (18)$$

Now, the plant and control parameters change with inductance variation, hence the model needs to be parameterized and analyzed over the entire range of variation for a complete picture of stability [32]. This is done by defining a parameter space, (mathematically termed as a *parameter hypercube* [43]) that includes the following dimensions.

1) Inductance variation factor $\boldsymbol{k_{Lx}}$

It is defined as the ratio of absolute inductance $L_x$ to nominal inductance $L_{\text{nom},x}$ at any instant, i.e.

$$k_{Lx} = \frac{L_x}{L_{\text{nom},x}} \quad (19)$$

bound by the allowable minimum inductance $L_{\min,x}$, *i.e.*, $\frac{L_{\min,x}}{L_{\text{nom},x}} \le k_{Lx} \le 1$.

2) Inductance estimation factor $\boldsymbol{k_{ex}}$

It is defined as the ratio of estimated inductance $L_{ex}$ to the absolute inductance $L_x$ at any instant, i.e.

$$k_{ex} = \frac{L_{ex}}{L_x} \quad (20)$$

with a reasonable limit of $0.8 \le k_{ex} \le 1.2$, considering the effect of hysteresis.

3) Line Impedance $\boldsymbol{L_L}$

It refers to the inductive transmission line impedance, the limit to which is typically defined by the maximum and minimum short-circuit ratio (SCR) [17] specifications for the inverter. A stiff grid is considered to be with an SCR = 500 and a weak

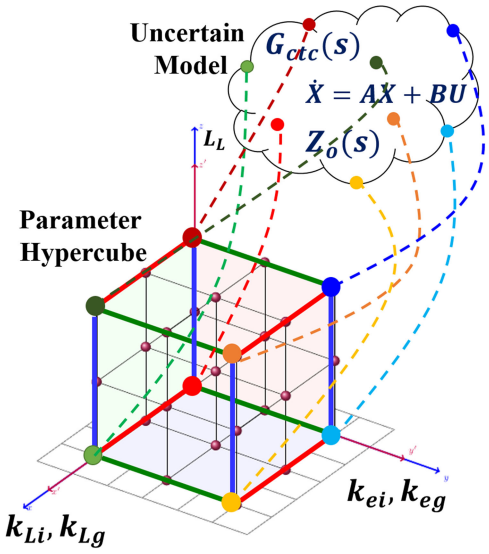


Fig. 6. Conceptual representation of a parameter hypercube and the uncertain model space with family of transfer functions.

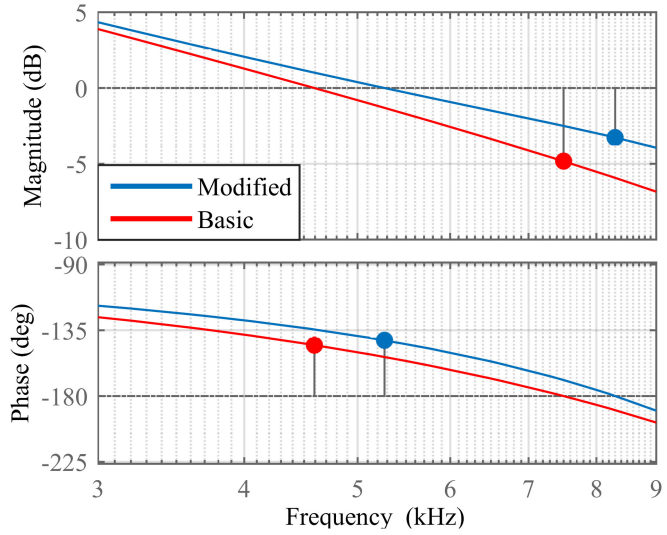


Fig. 7. Loop gain for control with and without modification and $0.2 \leq k_{Lx} \leq 1$ and $k_{ex} = 1$.

grid with SCR $= 10$–$15$, which corresponds to $L_L \approx 50\ \mu$H and $L_L = 1.7$–$2.5$ mH, respectively, for a 5 kW, 220 V, 60 Hz inverter.

The bounds on $k_{Lx}$ and $k_{ex}$ are assumed to be same for both $L_i$ and $L_g$ at any instant, based on the understanding that both would have the same average current profile under steady state. Moreover, it reduces the parameter space to a simple three-dimensional cuboid, which otherwise would become a complex five-dimensional hypercube. A family of models (17) and transfer functions for the parameter space are then derived from Fig. 5. A conceptual representation of the same is shown in Fig. 6. Each point $(k_{Lx},\ k_{ex}, L_L)$ on the parameter space corresponds to a set of model and transfer functions in an uncertain model space which can be further used for conventional stability analysis.

Gridding the parameter space and checking stability at discrete combinations of $(k_{Lx},\ k_{ex}, L_L)$ are feasible for a small parameter space. Alternative solutions have been presented for systems with large parameter space in [29], [32], and references therein, such that stability analysis with only a subset of parameter space would imply overall stability, but with limited applicability. Nevertheless, the parameter space considered here is usually very small due to physical and practical limitations. $k_{Lx}$ is limited by inductor-core saturation level for maximum current specification of the inverter, $k_{ex}$ is limited by the accuracy of the inductance estimation model, and $L_L$ is limited by international conformance standards for interconnection of inverters such as IEEE 1547.1 [1] (specifies SCR $\geq 20$ for conformance testing). Hence, selected combinations of $(k_{Lx},\ k_{ex}, L_L)$, by keeping one of the parameter constant while varying the other two, have been used in this paper to observe the pattern in stability margins through bode plots. A few points to note here are that the bode plots for analysis are shown maximum up to the Nyquist frequency, since the switching average model is valid only up to that frequency [15]. A switching average model corresponding to the basic controller (12) is also used for comparative analysis. However, the transfer function expressions for modified controller (16) are only shown. The steps for derivation of the transfer functions have been elaborated in Appendix A. The corresponding details for basic control are derived similarly, but not shown for brevity.

### A. *Current Tracking Capability* $(G_{\rm ctc})$

The controller being an inverter-side current feedback-based control, the tracking capability of $i_i$ to $i_{\rm ref}$ is investigated from the transfer function shown as follows:

$$G_{\rm ctc}\ (s) = \left.\frac{i_i}{i_{\rm ref}}\right|_{v_c=0} = \frac{k_0}{k_1 s + k_0} \tag{21}$$

where the coefficients are given by the following expressions:

$$\begin{aligned} k_0 &= \left(k_{ei} k_{Li} L_{{\rm nom},i} + k_{eg} k_{Lg} L_{{\rm nom},g}\right) G_d\ (s)\ f_s \\ k_1 &= k_{Li}\ L_{{\rm nom},i} + k_{Lg} L_{{\rm nom},g} G_d\ (s)\ G_{\rm avg}\ (s)\,. \end{aligned} \tag{22}$$

Assuming inductance estimation factor $k_{ex} = 1$ and inductance variation factor $0.2 \leq k_{Lx} \leq 1$, loop gain derived from (21) is shown in Fig. 7 (plot in BLUE). The loop gain derived similarly for basic control is also shown in Fig. 7 (plot in RED) and it is observed that a slightly higher bandwidth and better phase margin is obtained due to consideration of grid-side inductance. It is also observed from Fig. 7 that for a particular inductance estimation factor $k_{ex}$, current tracking is not affected with inductance variation. The magnitude and phase plots for different values of $k_{Lx}$ overlap with each other.

However, the phase margin does get affected with variation in $k_{ex}$ for a particular value of $k_{Lx}$, as shown in the phase margin versus inductance estimation factor plot in Fig. 8 for modified control.

Now, controller is not independent of the variations in terminal voltage $v_c$ because the control output impedance would interact with $C_g$ and $L_g$ and potentially lead to instability even in the absence of line impedance. This can be best analyzed through impedance-based stability analysis method [33].

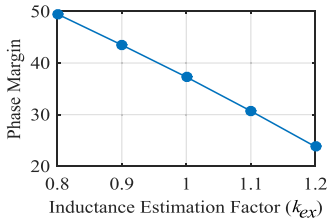


Fig. 8. Phase margin versus inductance estimation factor curves for control with modification and $0.8 \leq k_{ex} \leq 1.2$ at $k_{Lx} = 1$ and $k_{Lx} = 0.2$.

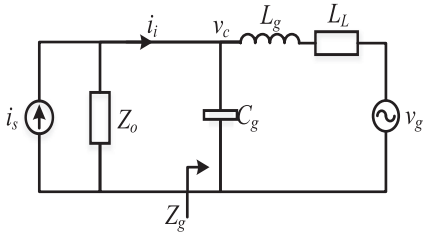


Fig. 9. Equivalent impedance model of inverter-side current controlled grid-connected inverter with *LCL* filter.

### B. Output Impedance Interaction ($Z_o$)

The equivalent impedance model for grid-connected inverter with inverter-side current feedback based-control is shown in Fig. 9.

The transfer function shown below represents the output impedance for modified control

$$Z_o\ (s) = -\frac{v_c}{i_i}\bigg|_{i_{\rm ref}=0} = -\frac{p_1 s + p_0}{q_2 s^2 + q_0} \tag{23}$$

where the coefficients are given by the following expressions:

$$\begin{aligned} p_0 &= \left(k_{ei} k_{Li} L_{{\rm nom},i} + k_{eg} k_{Lg} L_{{\rm nom},g}\right) G_d\ (s)\ f_s \\ p_1 &= k_{Li}\ L_{{\rm nom},i} + k_{Lg} L_{{\rm nom},g} G_d\ (s)\ G_{\rm avg}\ (s) \\ q_0 &= \left(1 + k_{eg} k_{Lg} L_{{\rm nom},g} C_g G_v\ (s)\right) G_d\ (s)\ G_{\rm avg}\ (s) - 1 \\ q_2 &= k_{Lg}\ L_{{\rm nom},g} C_g G_d\ (s)\ G_{\rm avg}\ (s)\ . \end{aligned} \tag{24}$$

The grid-side impedance as seen at the terminal of the controller is given by the following:

$$Z_g\ (s) = \frac{\left(k_{Lg} L_{{\rm nom},g} + L_L\right) s}{1 + C_g\left(k_{Lg} L_{{\rm nom},g} + L_L\right) s^2}\ . \tag{25}$$

Assuming the basic criteria for stable source and load are satisfied and according to impedance-based stability criterion [33], the system would remain stable if the impedance ratio $Z_g(s)/Z_o(s)$ satisfies the Nyquist criterion. With the assumption of a stiff grid, the output impedance $Z_o(s)$ (BLUE) and grid impedance $Z_g(s)$ (GREEN) plots for the first set of *LCL* parameters in Table I (i.e., $L_i = 1.2$ mH, $C_g = 5\ \mu$F, $L_g = 0.28$ mH) are shown in Fig. 10. The output impedance derived for basic control $Z_o'(s)$ is also shown in Fig. 10 (RED) for comparative analysis. It is observed from Fig. 10(a) that when filter inductors are at their nominal values, i.e., $k_{Lx} = 1$, $Z_o(s)$ intersects $Z_g(s)$ at two critical frequencies 3.55 and 4.48 kHz with a phase difference of $60.5^\circ$ and $-153.7^\circ$, respectively, indicating sufficient phase margin. Similarly, $Z_o'(s)$ intersects $Z_g(s)$ at 3.44

TABLE I
SYSTEM PARAMETERS OF INVERTER PROTOTYPE

| Parameters | Symbol | Values | |
|---|---|---|---|
| DC-link voltage | $v_{dc}$ | 360 ~ 400 V | |
| AC output voltage | $v_{g,rms}$ | 220 V | |
| Maximum rated power | $P_{rated}$ | 5 kW | |
| Line frequency | $f_0$ | 60 Hz | |
| Power Switch | SiC MOSFET C2M0025120D | $V_{DS}$ = 1200 V, $I_{D(TC=25°C)}$ = 90 A, and $R_{DS(on)}$ = 25 mΩ | |
| Switching Frequency | $f_s$ | 30 kHz | |
| Inverter-side Inductance | $L_i$ | 1.2 mH | 1.5 mH |
| Filter Capacitor | $C_g$ | 5 μF | 10 μF |
| Grid-side Inductance | $L_g$ | 0.28 mH | 0.25 mH |

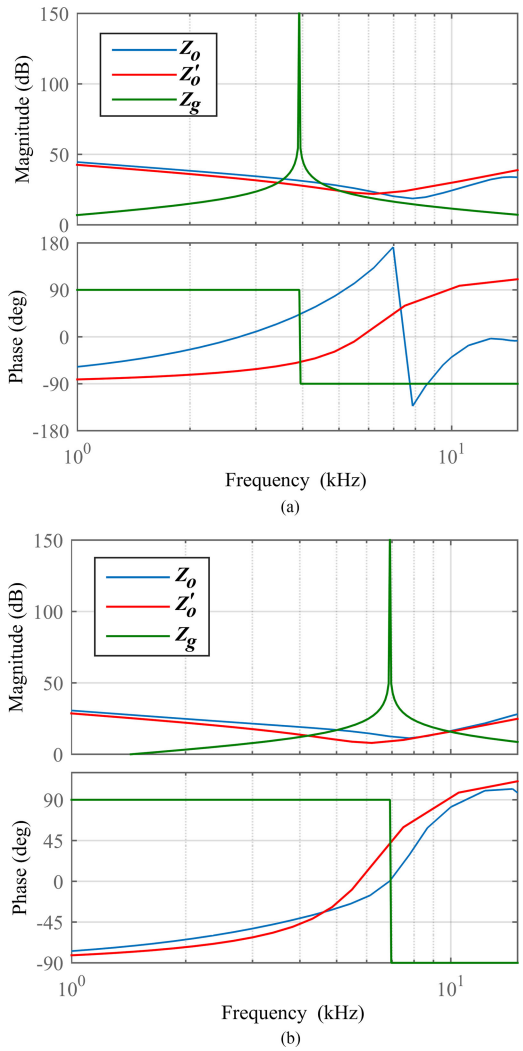


Fig. 10. Output impedance versus grid impedance for basic and modified control when connected to a stiff grid (SCR = 500) and inductance at (a) 100% and (b) 20% of nominal value.

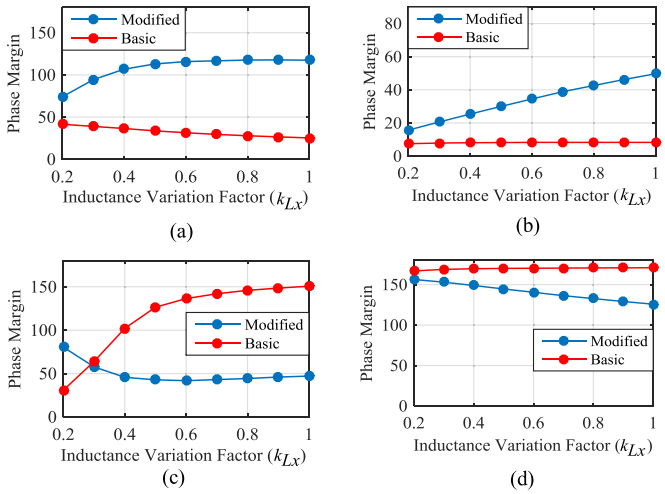


Fig. 11. Phase margins under wide variation of filter inductance derived from output impedance versus grid impedance plots for basic and modified control at the first critical frequency when connected to (a) stiff grid ($L_L \approx 50\ \mu$H) and (b) weak grid ($L_L \approx 2.0$ mH) and at the second critical frequency when connected to (c) stiff grid ($L_L \approx 50\ \mu$H) and (d) weak grid ($L_L \approx 2.0$ mH).

and 5.07 kHz with a phase difference of $146.0^\circ$ and $-68.2^\circ$, respectively, indicating good phase margin. And it is observed from Fig. 10(b) that when filter inductors are at 20% of their nominal values, i.e., $k_{Lx} = 0.2$, $Z_o(s)$ intersects $Z_g(s)$ at 5.04 and 9.87 kHz with a phase difference of $119.2^\circ$ and $-169.2^\circ$, respectively, indicating sufficient phase margin, while $Z_o'(s)$ intersects $Z_g(s)$ at 4.21 and 9.99 kHz with phase difference of $133.2^\circ$ and $-182.1^\circ$ respectively, with almost no phase margin at 9.99 kHz. It is also observed that $|\frac{Z_g(s)}{Z_o(s)}| > 1$ for basic control at 9.78 kHz, where $\Delta\varphi = -180.0^\circ$ indicating instability. It can be confirmed from the above observation that the prediction of stability based on only the nominal value of filter inductance would not be sufficient.

The second set of *LCL* parameters in Table I (i.e., $L_i = 1.5$ mH, $C_g = 10\ \mu$F, $L_g = 0.25$ mH) is also used to observe the relative stability margin for both basic and modified control over the entire range of filter inductance variation. A comparative plot of the phase margins at both the critical frequencies as $k_{Lx}$ varies from 0.2 to 1.0 when connected to a stiff grid (SCR $\approx$ 500) and to a weak grid (SCR $\approx$ 12) is shown in Fig. 11. It can be observed that the phase margin is comparatively higher with modified control even with drop in filter inductance and in the presence of line impedance at the first critical frequency. Although the phase margin at the second critical frequency is observed to be better for basic control, the overall balance of phase margins is better for modified control. Hence, modified control could be considered to be relatively stable than basic control. It is also observed that the phase margin varies a lot with filter inductance variation in the presence of line impedance. This again confirms that analysis done with nominal value of inductance would not be sufficient.

## VI. Experimental Verification

An inverter prototype based on the specifications of Table I is used for experimental verification. It was tested for different

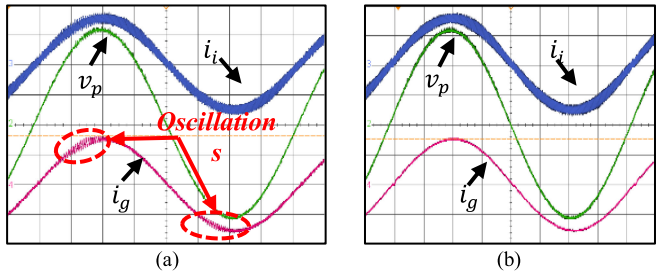


*($i_i$ and $i_g$: 20 A/div; $v_p$ 100 V/div; time:2 ms/div)*

Fig. 12. Measured waveforms of inverter current $i_i$, grid current $i_g$, PCC voltage $v_p$ with (a) basic and (b) modified control.

TABLE II
Test Results for Various Grid-Voltage Harmonics and Line Impedance

| Case | Grid-Voltage Harmonics | | % in Grid Current for different Line Impedances | | | |
|---|---|---|---|---|---|---|
| | | | basic | | modified | |
| | Order | % | $L_L$ = 50 μH | $L_L$ = 2 mH | $L_L$ = 50 μH | $L_L$ = 2 mH |
| I | - | - | - | - | - | - |
| | **THD (%)** | **0.11** | **0.961** | **2.282** | **0.872** | **1.403** |
| II | 3 | 5.0 | 0.801 | 0.939 | 0.784 | 0.885 |
| | 5 | 5.0 | 1.617 | 1.794 | 1.530 | 1.680 |
| | 7 | 3.0 | 1.245 | 1.506 | 1.204 | 1.437 |
| | 9 | 2.5 | 1.428 | 1.977 | 1.365 | 1.854 |
| | 11 | 2.0 | 1.457 | 2.198 | 1.358 | 1.997 |
| | **THD (%)** | **11.2** | **3.059** | **4.839** | **2.914** | **3.874** |

levels of grid-voltage harmonics and inductive line impedance. The test scenarios for grid-voltage harmonics were generated from a programmable ac source, Chroma 61512 (with an internal output inductance of about 50 $\mu$H) and the harmonics were measured using a power analyzer, WT1600.

### A. Effect of Modifications on Steady-State Stability

The first set of *LCL* parameters specified in Table I (i.e., $L_i = 1.2$ mH, $C_g = 5\ \mu$F, $L_g = 0.28$ mH) is used for this test scenario and molybdenum permalloy cores are used for filter inductors so as to allow 80% drop in inductance from nominal value at rated current. The inverter was tested with both basic and modified controls and the corresponding waveforms are shown in Fig. 12. It is observed that without modifications, the current waveforms have oscillations toward the peak, where inductance drops close to 20% of the nominal value. This confirms the stability analysis done in the previous section, where it was predicted that without modification the system would be unstable when inductance drops to 20% of the nominal value.

### B. Effect of Modifications on Grid-Current Harmonics

The second set of *LCL* parameters specified in Table I (i.e., $L_i = 1.5$ mH, $C_g = 10\ \mu$F, $L_g = 0.25$ mH) is used for various test scenarios. The test conditions and results are tabulated in Table II. The corresponding waveforms are also shown in Fig. 13. It can be observed that the grid-injected harmonics with modified control is comparatively less even in the presence of line impedance and grid-voltage harmonics. This confirms the effect of modifications on grid-voltage harmonic rejection.

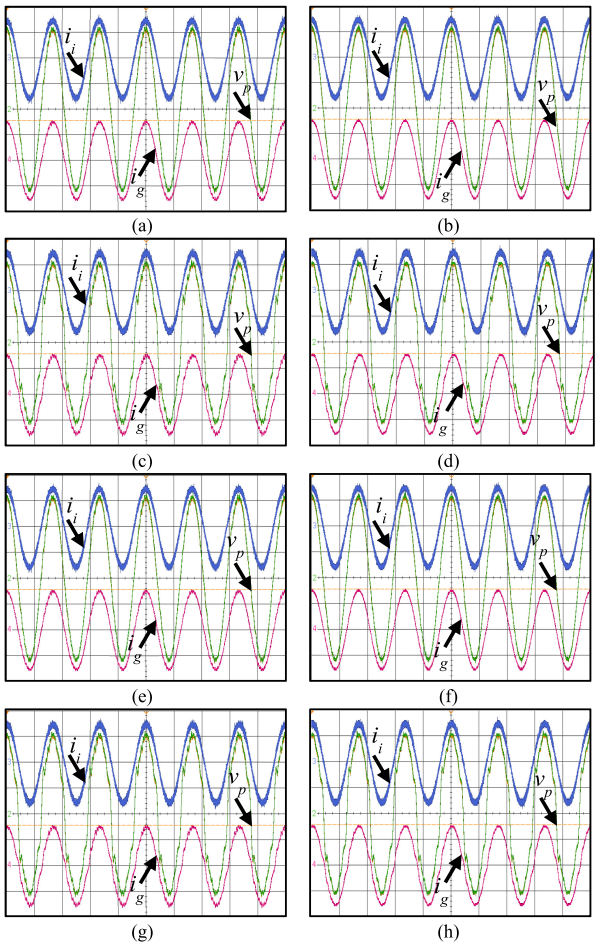


Fig. 13. Measured waveforms of inverter current $i_i$, grid current $i_g$, and PCC voltage $v_p$ with line inductance $L_L = 50\ \mu$H, Case I: (a) basic and (b) modified, Case II: (c) basic and (d) modified and with line inductance $L_L = 2$ mH, Case I: (e) basic and (f) modified, Case II: (g) basic and (h) modified.

### C. Effect of Modifications on Resonance Damping

With *LCL* parameters as $L_i = 1.5$ mH, $C_g = 10\mu$F, $L_g = 0.25$ mH and line inductance as $L_L = 2.0$ mH, the resonant frequency moves to the region between 17th and 28th harmonic orders due to inductance variation. And it can be observed from the corresponding harmonic spectrum, shown in Fig. 14 for both Case I and Case II of Table II, that the harmonics in the region are significantly suppressed in modified control. This confirms the effect of modifications on resonance damping.

### D. Effect of Consideration of Grid-Side Filter Inductance Variation on Control

The modified control law is applied with and without considering the variation in grid-side inductance. The corresponding measured waveforms under steady state are shown inFig. 15. When grid-side inductance variation is not taken into consideration in the control gain, severe current oscillations are observed near the peak where filter inductors are at around 20% of their nominal values. The oscillations, however, gradually

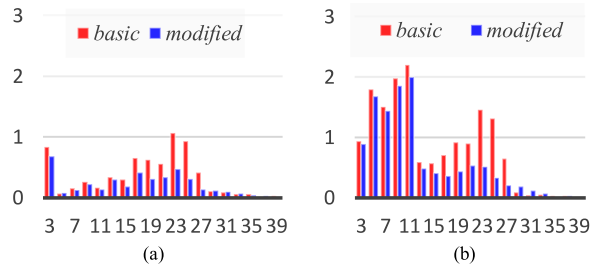


Fig. 14. Harmonic spectrum of grid current $i_g$ with line inductance $L_L = 2$ mH. (a) Case I. (b) Case II.

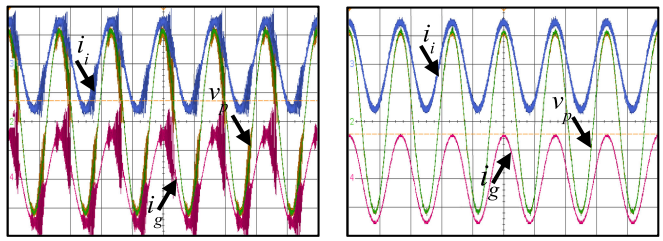


Fig. 15. Measured waveforms of inverter current $i_i$, grid current $i_g$, and PCC voltage $v_p$. (a) Without. (b) With consideration of grid-side filter inductance variation.

damp out as filter inductors reach its nominal value closer to the zero-crossing. This confirms the importance of considering the variation in grid-side inductance as well in the control.

### E. Effect of Variable Structure Inductance Estimation Model on Transient-State Stability

To validate the importance of variable structure inductance estimation model in Section III, various step-down responses near the peak, where inductance is minimum, are done. During a step-down of 5–4 kW or 5–3 kW near the peak, shown in Fig. 16(a) and (b), respectively, the estimated inductance from anhysteretic curve fit polynomial would vary from the absolute inductance leading to longer settling times. However, during a large step-down of 5–1 kW, the system enters protection due to filter capacitor voltage overshoot, as shown in Fig. 16(c). This is because of a larger discrepancy between the estimated inductance from anhysteretic curve fit polynomial and absolute inductance. After including the logic for variable structure inductance estimation model into control, the step-down response for 5–1 kW remains stable with very small capacitor voltage overshoot as shown in Fig. 16(d). This confirms the effectiveness of variable structure filter inductance estimation model in dealing with large step-down transient response.

## VII. Conclusion

A direct digital control method that can deal with wide variation in both inverter-side and grid-side inductance due to soft magnetic powder core material has been introduced in this paper. The rationale behind introducing a variable-structure

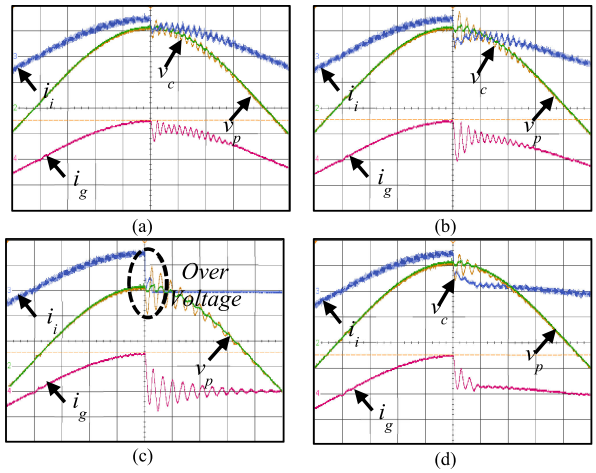


Fig. 16. Measured waveforms of inverter current $i_i$, grid current $i_g$, and capacitor voltage $v_c$ and PCC voltage $v_p$ during step-down near the peak from 5 kW to (a) 4 kW, (b) 3 kW, and (c) 1 kW without variable structure inductance estimation model and (d) step-down near the peak from 5 to 1kW with variable structure inductance estimation model.

inductance estimation model to deal with large-signal transient response has been discussed. And the limitation of conventional stability analysis based on nominal value of filter inductance in predicting instabilities has also been discussed. To investigate system stability over a wide range of filter inductance variation, impedance-based stability analysis method applied to a parameterized switching average model has been proposed. Experimental results have been shown to validate the proposed control and stability analysis approach. The proposed control method would enable power engineers to incorporate soft magnetic powder core-based filter inductors into inverter-based applications. The parametric stability analysis method will also be able to provide better insight into designing appropriate inductor cores and compensation gain, so as to ensure stability over the entire range of operation.

## Appendix A
## Derivations of Transfer Functions for Stability Analysis

From the control block diagram shown in Fig. 5, voltage at the inverter terminals $v_{\rm inv}$ is derived to be as follows:

$$\begin{aligned} v_{\rm inv} &= (2d-1)\ G_d v_{\rm dc} \\ &= \left( G_{\rm avg} v_p + \frac{L_{eT}}{T_s}\left(i_{\rm ref} - i_i\right) + L_{eg} C_g G_{\rm avg} G_v v_c \right) G_d \\ &= \Bigg( \left(1 + L_{eg} C_g G_v + s^2 L_g C_g\right) G_{\rm avg} v_c \\ &\qquad - s L_g G_{\rm avg} i_i + \frac{L_{ei} + L_{eg}}{T_s}\left(i_{\rm ref} - i_i\right) \Bigg) G_d. \end{aligned} \tag{26}$$

Now, again from the control block diagram, the expression for $i_i$ is derived to be as follows:

$$i_i = \frac{v_{\rm inv} - v_c}{s L_i}. \tag{27}$$

Substituting (26) in (27), the following expression is derived:

$$\begin{aligned} & v_c \left\{ \left(1 + L_{eg} C_g G_v + s^2 L_g C_g\right) G_{\rm avg} G_d - 1 \right\} \\ & \quad + i_{\rm ref} \left(L_{ei} + L_{eg}\right) G_d\ f_s = i_i \left\{ s \left(L_i + L_g G_{\rm avg} G_d\right) \right. \\ & \quad \left. + \left(L_{ei} + L_{eg}\right) G_d f_s \right\}. \end{aligned} \tag{28}$$

From (19) and (20), the following expressions are derived:

$$\begin{aligned} L_i &= k_{Li}\ L_{{\rm nom},i} \\ L_g &= k_{Lg}\ L_{{\rm nom},g} \\ L_{ei} &= k_{ei}\ \ L_i = k_{ei}\ k_{Li}.L_{{\rm nom},i} \\ L_{eg} &= k_{eg}\ \ L_g = k_{eg}\ k_{Lg}.L_{{\rm nom},g}. \end{aligned} \tag{29}$$

Substituting (29) in (28), the following expression is derived:

$$\begin{aligned} & v_c \left\{ \left(1 + k_{eg} k_{Lg}.L_{{\rm nom},g} C_g G_v + s^2 k_{Lg} L_{{\rm nom},g} C_g\right) G_{\rm avg} G_d - 1 \right\} \\ & \quad + i_{\rm ref} \left(k_{ei} k_{Li}.L_{{\rm nom},i} + k_{eg} k_{Lg}.L_{{\rm nom},g}\right) G_d\ f_s \\ & = i_i\ \left\{ s \left(k_{Li} L_{{\rm nom},i} + k_{Lg} L_{{\rm nom},g} G_{\rm avg} G_d\right) \right. \\ & \quad \left. + \left(k_{ei} k_{Li}.L_{{\rm nom},i} + k_{eg} k_{Lg}.L_{{\rm nom},g}\right) G_d f_s \right\}. \end{aligned} \tag{30}$$

Expressions (21) and (23) are then directly derived from (30).

## References


[1] *IEEE Standard Conformance Test Procedures for Equipment Interconnecting Distributed Resources With Electric Power Systems*, IEEE Std 1547.1-2005, Jul. 2005, pp. 1–62.

[2] *Electromagnetic Compatibility (EMC) - Part 3-12: Limits - Limits For Harmonic Currents Produced by Equipment Connected to Public Low-Voltage Systems With Input Current >16 A and < = 75 A Per Phase*, IEC Standard 61000-3.12, 2011, pp. 1–51.

[3] R. N. Beres, X. Wang, M. Liserre, F. Blaabjerg, and C. L. Bak, "A review of passive power filters for three-phase grid-connected voltage-source converters," *IEEE J. Emerg. Sel. Topics Power Electron.*, vol. 4, no. 1, pp. 54–69, Mar. 2016.

[4] M. Liserre, F. Blaabjerg, and S. Hansen, "Design and control of an LCL-filter-based three-phase active rectifier," *IEEE Trans. Ind. Appl.*, vol. 41, no. 5, pp. 1281–1291, Sep. 2005.

[5] J. Muhlethaler, M. Schweizer, R. Blattmann, J. W. Kolar, and A. Ecklebe, "Optimal design of LCL harmonic filters for three-phase PFC rectifiers," *IEEE Trans. Power Electron.*, vol. 28, no. 7, pp. 3114–3125, Jul. 2013.

[6] P. Channegowda and V. John, "Filter optimization for grid interactive voltage source inverters," *IEEE Trans. Ind. Electron.*, vol. 57, no. 12, pp. 4106–4114, Dec. 2010.

[7] Y. Lang, D. Xu, S. R. Hadianamrei, and H. Ma, "A novel design method of LCL type utility interface for three-phase voltage source rectifier," in *Proc. IEEE 36th Power Electron. Spec. Conf.*, Jun. 2005, pp. 313–317.

[8] R. N. Beres, X. Wang, F. Blaabjerg, M. Liserre, and C. L. Bak, "Optimal design of high-order passive-damped filters for grid-connected applications," *IEEE Trans. Power Electron.*, vol. 31, no. 3, pp. 2083–2098, Mar. 2016.

[9] J. Dannehl, F. W. Fuchs, S. Hansen, and P. B. Thogersen, "Investigation of active damping approaches for pi-based current control of grid-connected pulse width modulation converters with LCL filters," *IEEE Trans. Ind. Appl.*, vol. 46, no. 4, pp. 1509–1517, Jul. 2010.

[10] X. Wang, F. Blaabjerg, and P. C. Loh, "Analysis and design of grid-current-feedback active damping for LCL resonance in grid-connected voltage source converters," in *Proc. IEEE Energy Convers. Congr. Expo.*, Sep. 2014, pp. 373–380.

[11] X. Li, X. Wu, Y. Geng, X. Yuan, C. Xia, and X. Zhang, "Wide damping region for LCL-type grid-connected inverter with an improved capacitor-current-feedback method," *IEEE Trans. Power Electron.*, vol. 30, no. 9, pp. 5247–5259, Sep. 2015.
[12] J. Dannehl, M. Liserre, and F. W. Fuchs, "Filter-based active damping of voltage source converters with *LCL* filter," *IEEE Trans. Ind. Electron.*, vol. 58, no. 8, pp. 3623–3633, Aug. 2011.
[13] R. Peña-Alzola, M. Liserre, F. Blaabjerg, R. Sebastián, J. Dannehl, and F. W. Fuchs, "Systematic design of the lead-lag network method for active damping in LCL-filter based three phase converters," *IEEE Trans. Ind. Informat.*, vol. 10, no. 1, pp. 43–52, Feb. 2014.
[14] C. P. Dick, S. Richter, M. Rosekeit, J. Rolink, and R. W. D. Doncker, "Active damping of LCL resonance with minimum sensor effort by means of a digital infinite impulse response filter," in *Proc. Eur. Conf. Power Electron. Appl.*, Sep. 2007, pp. 1–8.
[15] D. Yang, X. Ruan, and H. Wu, "Impedance shaping of the grid-connected inverter with LCL filter to improve its adaptability to the weak grid condition," *IEEE Trans. Power Electron.*, vol. 29, no. 11, pp. 5795–5805, Nov. 2014.
[16] M. A. Swihart, "Inductor cores–material and shape choices," *Magnetics*, 2004. [Online]. Available: www. mag-inc. com
[17] T. F. Wu, M. Misra, L. C. Lin, and C. W. Hsu, "An improved resonant frequency based systematic LCL filter design method for grid-connected inverter," *IEEE Trans. Ind. Electron.*, vol. 64, no. 8, pp. 6412–6421, Aug. 2017.
[18] T. F. Wu, L. C. Lin, N. Yao, Y. K. Chen, and Y. C. Chang, "Extended application of D-Σ digital control to a single-phase bidirectional inverter with an LCL filter," *IEEE Trans. Power Electron.*, vol. 30, no. 7, pp. 3903–3911, Jul. 2015.
[19] T. F. Wu, M. Misra, L. C. Lin, and Y. H. Huang, "A modified division-summation digital control for grid-connected inverter with wide inductance variation of LCL filter," in *Proc. IEEE Appl. Power Electron. Conf. Expo.*, Mar. 2017, pp. 2781–2787.
[20] J. Wang, J. D. Yan, L. Jiang, and J. Zou, "Delay-dependent stability of single-loop controlled grid-connected inverters with LCL filters," *IEEE Trans. Power Electron.*, vol. 31, no. 1, pp. 743–757, Jan. 2016.
[21] W. Xia and J. Kang, "Stability of LCL-filtered grid-connected inverters with capacitor current feedback active damping considering controller time delays," *J. Modern Power Syst. Clean Energy*, vol. 5, no. 4, pp. 584–598, Jul. 2017.
[22] J. Wang and J. D. Yan, "Using virtual impedance to analyze the stability of LCL-filtered grid-connected inverters," in *Proc. IEEE Int. Conf. Ind. Technol.*, Mar. 2015, pp. 1220–1225.
[23] Y. Tang, C. Yoon, R. Zhu, and F. Blaabjerg, "Generalized stability regions of current control for LCL-filtered grid-connected converters without passive or active damping," in *Proc. IEEE Energy Convers. Congr. Expo.*, Sep. 2015, pp. 2040–2047.
[24] M. Liserre, R. Teodorescu, and F. Blaabjerg, "Stability of photovoltaic and wind turbine grid-connected inverters for a large set of grid impedance values," *IEEE Trans. Power Electron.*, vol. 21, no. 1, pp. 263–272, Jan. 2006.
[25] S. Eren, M. Pahlevaninezhad, A. Bakhshai, and P. K. Jain, "Composite nonlinear feedback control and stability analysis of a grid-connected voltage source inverter with LCL filter," *IEEE Trans. Ind. Electron.*, vol. 60, no. 11, pp. 5059–5074, Nov. 2013.
[26] B. Zhou, "Stability analysis of non-linear time-varying systems by lyapunov functions with indefinite derivatives," *IET Control Theory Appl.*, vol. 11, no. 9, pp. 1434–1442, 2017.
[27] N. Tan and D. P. Atherton, "A new approach to the stability of nonlinear systems with uncertain plant parameters," in *Proc. Amer. Control Conf.*, Jun. 2003, vol. 3, pp. 1843–1848.
[28] B. K. Sahu, M. M. Gupta, and B. Subudhi, "Stability analysis of nonlinear systems using dynamic-routh's stability criterion: A new approach," in *Proc. Int. Conf. Adv. Comput., Commun. Informat.*, Aug. 2013, pp. 1765–1769.
[29] J. Ackermann, "Uncertainty structures and robust stability analysis," in *Proc. Eur. Control Conf.*, 1991, vol. 3, pp. 2318–2327.
[30] D. Halliday, R. Resnick, and J. Walker, *Fundamentals of Physics*, 10th ed. Hoboken, NJ, USA: Wiley, 2010, ch. 28–31.
[31] G. L. Johnson, *Solid State Tesla Coil*. Lawrence, Kansas, USA: Kansas State Univ. Press, Dec. 2001, ch. 4.
[32] M. P. Polis, A. W. Olbrot, and M. Fu, "An overview of recent results on the parametric approach to robust stability," in *Proc. 28th IEEE Conf. Decision Control*, Dec. 1989, vol. 1, pp. 23–29.
[33] J. Sun, "Impedance-based stability criterion for grid-connected inverters," *IEEE Trans. Power Electron.*, vol. 26, no. 11, pp. 3075–3078, Nov. 2011.
[34] *Magnetic Powder Cores-Product Catalog*, Ver. 12, Chang Sung Corporation, Incheon, South Korea, 2017.
[35] *Powder Cores-Product Catalog*, Magnetics, Pittsburgh, PA, USA, 2017.
[36] Z. Xin, X. Wang, P. C. Loh, and F. Blaabjerg, "Realization of digital differentiator using generalized integrator for power converters," *IEEE Trans. Power Electron.*, vol. 30, no. 12, pp. 6520–6523, Dec. 2015.
[37] D. M. V. de Sype, K. D. Gusseme, A. P. V. den Bossche, and J. A. A. Melkebeek, "A sampling algorithm for digitally controlled boost pfc converters," *IEEE Trans. Power Electron.*, vol. 19, no. 3, pp. 649–657, May 2004.
[38] A. Bermúdez, D. Gómez, and P. Salgado, *An Introduction to Nonlinear Magnetics. Hysteresis*. Cham, Switzerland: Springer, 2014. [Online]. Available: https://doi.org/10.1007/978-3-319-02949-8_11
[39] B. W. K.J. Astrom, *Adaptive Control*, 2nd ed. New York, NY, USA: Dover, 2008.
[40] R. Erickson and D. Maksimovic, *Fundamentals of Power Electronics*. New York, NY, USA: Springer, 2007.
[41] Y. S. Xi-Fan Wang and M. Irving, *Modern Power Systems Analysis*. New York, NY, USA: Springer, 2008, ch. 8.
[42] J. L. Agorreta, M. Borrega, J. López, and L. Marroyo, "Modeling and control of *n* -paralleled grid-connected inverters with LCL filter coupled due to grid impedance in pv plants," *IEEE Trans. Power Electron.*, vol. 26, no. 3, pp. 770–785, Mar. 2011.
[43] A. Sideris and R. S. S. Pena, "Fast computation of the multivariable stability margin for real interrelated uncertain parameters," in *Proc. Amer. Control Conf.*, Jun. 1988, pp. 1483–1488.

**Tsai-Fu Wu** (S'88–M'91–SM'98) received the B.S. degree in electronic engineering from National Chiao-Tung University, Hsinchu, Taiwan, in 1983, the M.S. degree in electrical and computer engineering from Ohio University, Athens, OH, USA, in 1988, and the Ph.D. degree in electrical engineering and computer science from the University of Illinois, Chicago, IL, USA, in 1992.

From 1993 to 2012, he was with the Department of Electrical Engineering, National Chung Cheng University, Chia-Yi, Taiwan. He is currently a Distinguished Professor with the Department of Electrical Engineering, National Tsing Hua University, Hsinchu, Taiwan. He used to serve as the Department Head for six years and the Vice President of the university for three years. His current research interests include the development and modeling of power converters, design and development of direct digital control with D-Σ processes for single-phase and three-phase converters with grid connection, rectification, APF, power balancing and UPS functions, and design of resonant converters for ultrasonic cutter, ozone generator, remote-plasma-source, and electrical-surgery-unit applications. He has been involved in power electronics education since 1993 and has authored and coauthored more than 250 referred technical papers and 7 books (in Chinese), focusing more on development of power converters, controls for various power electronics applications and key power modules for harmonized ac/dc microgrids. He also owns 30 patents.

Dr. Wu has been an Associate Editor for the IEEE TRANSACTIONS ON POWER ELECTRONICS since 2000. He was the Guest Editor-in-Chief for the IEEE TRANSACTIONS ON POWER ELECTRONICS in "DC Distribution Systems" from 2012 to 2013. He was the recipient of seven Best Paper Awards from the Taipei Power Electronics Association in 2010–2016, and one excellent paper award from IEEE PEAC'14. In 2006 and 2014, he was awarded as an outstanding researcher by the Ministry of Science and Technology, Taiwan.

**Mitradatta Misra** was born in India, in 1985. He received the B.Tech. degree in electrical engineering from the Biju Patnaik Univeristy of Technology, Rourkela, India, in 2008. He is currently working toward the Ph.D. degree at the Department of Electrical Engineering, National Tsing Hua University, Hsinchu, Taiwan.

From 2008 to 2014, he was with Infosys Limited, India. His research interests include design and control of inverters with *LCL* filters and electric motor emulation using power converters.

**Ying-Yi Jhang** was born in Taiwan, in 1990. He received the B.S. degree from National Taiwan University of Science and Technology, Taipei, Taiwan, in 2013, and the M.S. degree from National Tsinghua University, Hsinchu, Taiwan, in 2015, both in electrical engineering.

His research interests include design and implementation of three-phase three-wire inverters for grid-connection with DSP-based control and the development of dc-microgrid distribution systems.

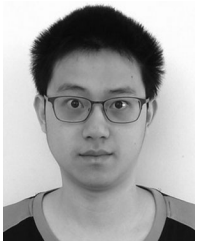

**Yen-Hsiang Huang** was born in Taiwan, in 1993. He received the B.S. degree from National Tsing Hua University, Hsinchu, Taiwan, in 2015. He is currently working toward the Ph.D. degree at the Department of Electrical Engineering, National Tsing Hua University, Hsinchu.

His main research interests include grid-connected inverters.

**Li-Chiun Lin** was born in Taiwan, in 1986. He received the B.S. degree from the National Kaohsiung University of Science and Technology, Kaohsiung City, Taiwan, in 2009, and the Ph.D. degree from National Chung Cheng University, Chiayi, Taiwan, in 2014, both in electrical engineering.

He is currently a Postdoctoral Researcher with the Department of Electrical Engineering, National Tsing Hua University, Hsinchu, Taiwan. His research interests include design and implementation of three-phase four-wire inverters for UPS applications with DSP-based control and the development of dc-microgrid distribution systems.